

Three-component fermions with surface Fermi arcs in tungsten carbide

J.-Z. Ma^{1,2}, J.-B. He^{1,3}, Y.-F. Xu^{1,2}, B. Q. Lv^{1,2}, D. Chen^{1,2}, W.-L. Zhu^{1,2}, S. Zhang¹, L.-Y. Kong^{1,2}, X. Gao^{1,2}, L.-Y. Rong^{2,4}, Y.-B. Huang^{1,4}, P. Richard^{1,2,5}, C.-Y. Xi⁶, E. S. Choi⁷, Y. Shao^{1,2}, Y.-L. Wang^{1,2,5}, H.-J. Gao^{1,2,5}, X. Dai^{1,2,5}, C. Fang¹, H.-M. Weng^{1,5}, G.-F. Chen^{1,2,5*}, T. Qian^{1,5*} and H. Ding^{1,2,5*}

Topological Dirac and Weyl semimetals not only host quasiparticles analogous to the elementary fermionic particles in high-energy physics, but also have a non-trivial band topology manifested by gapless surface states, which induce exotic surface Fermi arcs^{1,2}. Recent advances suggest new types of topological semimetal, in which spatial symmetries protect gapless electronic excitations without high-energy analogues^{3–11}. Here, using angle-resolved photoemission spectroscopy, we observe triply degenerate nodal points near the Fermi level of tungsten carbide with space group $P\bar{6}m2$ (no. 187), in which the low-energy quasiparticles are described as three-component fermions distinct from Dirac and Weyl fermions. We further observe topological surface states, whose constant-energy contours constitute pairs of 'Fermi arcs' connecting to the surface projections of the triply degenerate nodal points, proving the non-trivial topology of the newly identified semimetal state.

The standard model predicts three types of fermionic elementary particle in the universe, Dirac, Weyl and Majorana fermions. So far, only Dirac fermions have been identified and the existence of Weyl and Majorana fermions has not been confirmed experimentally in high-energy physics. In recent years, it has been realized that crystal symmetry-protected gapless electronic excitations in condensed-matter systems are analogous to these elementary particles^{1,2,12–14}. For example, the excitations near four- and two-fold degenerate nodal points in the electronic structures can be described by the Dirac and Weyl equations, respectively^{1,2}. Materials hosting Dirac and Weyl nodes near the Fermi level (E_F), called Dirac and Weyl semimetals, have been predicted theoretically^{1,2,15–18} and discovered experimentally^{19–23}. One hallmark of Dirac and Weyl semimetals is the surface Fermi arcs connecting to the surface projection points of bulk Dirac or Weyl nodes^{1,2,15–18,20–23}. The connection in Weyl semimetals is topologically protected by non-zero topological charges of Weyl nodes^{1,15–18,20–23}. By contrast, the connection in Dirac semimetals is not protected since Dirac nodes have zero topological charge, and the Fermi arcs can be deformed into a closed Fermi surface (FS) by a strong surface potential or an arbitrarily small bulk perturbation that preserves the Dirac nodes and all of the symmetries^{2,24–27}. However, the surface states (SSs) in Dirac semimetals do have topological character manifested by the gapless SS bands connecting

bulk valence and conduction bands, which are protected by the two-dimensional (2D) topological properties on time-reversal invariant planes in the Brillouin zone (BZ)^{24,26}.

In addition to four- and two-fold degeneracy, it has been shown that space-group symmetries in crystals may protect other types of degenerate point, near which the quasiparticle excitations are not the analogues of any elementary fermions described in the standard model. Theory has proposed three-, six- and eight-fold degenerate points at high-symmetry momenta in the BZ in several specific non-symmorphic space groups^{3,4,10,11}, where the combination of non-symmorphic symmetries and other point symmetries leads to three-, six- and eight-dimensional irreducible representations. Theory has also proposed that in a symmorphic space group $P\bar{6}m2$ (no. 187) with the tungsten carbide (WC)-type structure, the combination of rotation and mirror symmetries may protect three-fold degenerate points on the high-symmetry line^{5–9}, which are accidental degeneracy points between the bands of one- and two-dimensional irreducible representations due to band inversion.

In this work, we investigate the three-fold degeneracy proposed in the symmorphic system WC^{6–9}. As illustrated in Fig. 1a, the three-fold degeneracy lies in an intermediate state between Dirac and Weyl states. Recovering inversion symmetry makes two triply degenerate nodal points (TPs) merging into a single Dirac node, while applying a Zeeman field along the rotation axis drives a TP into two Weyl nodes^{5–9}. In contrast to isolated Dirac and Weyl nodes, the pair of TPs is connected by a doubly degenerate band. For an arbitrary E_F near the TPs, the two FS pockets that contain the TPs are touching. Therefore, the topological charge of the TPs in WC is undefined. This is topologically distinct from the TPs enforced by non-symmorphic symmetries, which have non-zero topological charge⁴.

The presence of TPs was first demonstrated by our previous angle-resolved photoemission spectroscopy (ARPES) measurements on MoP, which is isostructural to WC²⁸. MoP has recently been reported to have extremely low resistivity and high carrier mobility, although the TPs are far below E_F and the three-component fermions are thought to have little contribution to low-energy quasiparticle excitations²⁹. Since topological SSs are not observed in MoP²⁸, evidence of the topological nature for the TP semimetal state is still lacking. In this work, using ARPES we clearly observe the TPs near E_F in the electronic structure of WC. The low-energy quasiparticles on the

¹Beijing National Laboratory for Condensed Matter Physics and Institute of Physics, Chinese Academy of Sciences, Beijing, China. ²School of Physics, University of Chinese Academy of Sciences, Beijing, China. ³College of Physics and Electronic Engineering, Nanyang Normal University, Nanyang, China.

⁴Shanghai Synchrotron Radiation Facility, Shanghai Institute of Applied Physics, Chinese Academy of Sciences, Shanghai, China. ⁵Collaborative Innovation Center of Quantum Matter, Beijing, China. ⁶Anhui Province Key Laboratory of Condensed Matter Physics at Extreme Conditions, High Magnetic Field Laboratory of the Chinese Academy of Sciences, Hefei, Anhui, China. ⁷National High Magnetic Field Laboratory, Tallahassee, FL, USA. J.-Z. Ma, J.-B. He and Y.-F. Xu contributed equally to this work. *e-mail: gfchen@iphy.ac.cn; tqian@iphy.ac.cn; dingh@iphy.ac.cn

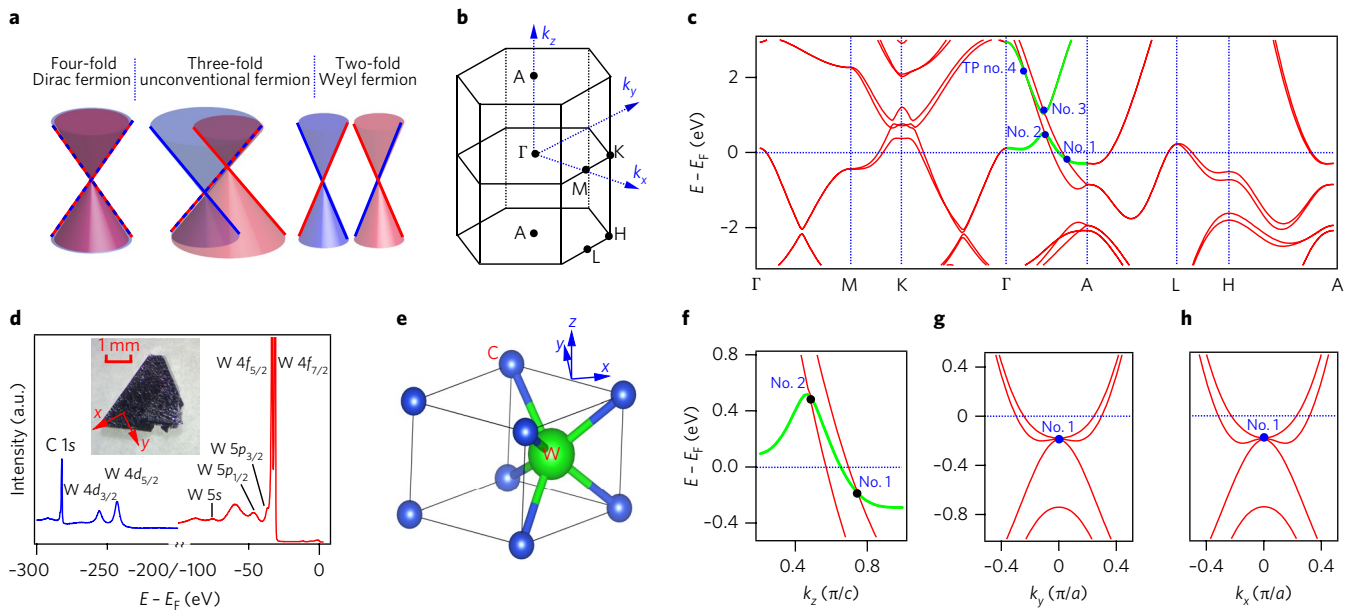


Fig. 1 | Electronic structure of TPs in WC. **a**, Schematic plots of the band structures of a four-fold Dirac fermion, a three-fold unconventional fermion, and a two-fold Weyl fermion. **b**, Bulk BZ with high-symmetry points. **c**, Calculated bulk band structure along high-symmetry lines. The green curves represent the doubly degenerate bands along Γ -A that cross the singly degenerate bands, forming the four TPs (no. 1 to no. 4) indicated as blue dots. **d**, Core-level photoemission spectrum showing the characteristic peaks of W and C elements. The inset shows a typical triangular WC single crystal. **e**, Crystal structure of WC in one unit cell. **f-h**, Calculated bands along k_z (**f**), k_y (**g**) and k_x (**h**) through TP no. 1.

FSs containing the TPs are described as three-component fermions. Very recently, we have observed quite strong anisotropic longitudinal magnetoresistance in WC³⁰, which is likely to be related to the behaviour of three-component fermions under magnetic fields applied along different directions, as theoretically proposed⁶. This is in sharp contrast to the isotropic longitudinal magnetoresistance observed in Dirac and Weyl semimetals^{31,32}. Moreover, we identify surface Fermi arcs connecting to the projections of the TPs on the (100) surface of WC. It should be noted that the connection in WC is not protected due to the undefined topological charge of the TPs. We thus classify them as Dirac-type Fermi arcs, which are distinct from the Weyl-type Fermi arcs whose connection is protected by non-zero topological charges. As with Dirac semimetals, our study reveals that WC hosts gapless SS bands protected by the bulk band topology on the time-reversal invariant $k_z = \pi$ planes, explicitly demonstrating the non-trivial topology of the semimetallic phase of WC.

Band calculations of WC indicate an inversion between the d_{z^2} and e_g states at the A point, leading to a band crossing along Γ -A⁶⁻⁹. When spin-orbit coupling (SOC) is considered, these bands along Γ -A are reconstructed into two doubly degenerate $|J_z| = 1/2$ bands and two singly degenerate $|J_z| = 3/2$ bands⁶. The C_{3z} symmetry protects the crossing points between the $|J_z| = 1/2$ and $3/2$ bands, resulting in four TPs on the Γ -A line (Fig. 1c). In the plane perpendicular to Γ -A, three singly degenerate bands converge at a TP (Fig. 1g,h). The strong SOC of W 5d electrons causes large band splitting in WC as compared with MoP, which facilitates the identification of TPs and the investigation of associated topological properties in ARPES experiments.

The measured samples have a typical triangular shape. The triangle surface is the (001) plane and its edge is along the [010] direction, as illustrated in the inset of Fig. 1d. We obtained mirror-like (001) and (100) surfaces on a macroscopic scale ($\sim 0.1 \times 0.1 \text{ mm}^2$) by cleavage. However, in the ARPES experiments with vacuum ultraviolet (VUV) light, we did not observe any dispersive bands on both surfaces. In contrast, we observe

clear band dispersions with photon energy ($h\nu$) larger than 300 eV. To understand this phenomenon, we measured the (100) cleavage surface with scanning tunnelling microscopy (STM). A typical STM topographic image is shown in Fig. 4g. We did not observe any ordered lattice in all of the measured regions on several cleaved surfaces, indicating that the top layer is disordered and should not support a well-defined band structure. As the photoelectrons excited by VUV light have a mean free path on the order of a few ångströms, we detect the electronic states only in the disordered layer in the VUV ARPES experiments. By contrast, the photoelectrons excited by soft x-ray light have a much longer mean free path³³, and therefore using soft x-ray ARPES we are able to detect the well-defined band structure in the ordered lattice beneath the disordered layer.

The measured electronic structure exhibits a periodic modulation with varying $h\nu$. Figure 2d,e plots the FSs recorded with two different $h\nu$ values on the (001) surface, which are qualitatively consistent with the calculated bulk FSs in the $k_z = 0$ (Fig. 2h) and π (Fig. 2i) planes, respectively. The ARPES results exhibit four FSs located around Γ , K, A and L. Although the calculations indicate that SOC splits each FS in two, the splitting is not resolved in the FSs measured by ARPES. To further characterize the FS structures, we have performed quantum oscillation (QO) measurements with magnetic fields (B) up to 38 tesla (Fig. 2c), which is a powerful experimental technique to measure the extreme cross-sections of FSs in the planes perpendicular to B ³⁴. The fast Fourier transform (FFT) spectra of the QO data with $B \parallel c$ exhibit eight principal frequencies F_1 - F_8 , which should correspond to the split FSs at Γ , L, K and A in the k_x - k_y planes. Considering the cross-sectional areas, the two double-peak structures $F_{1,2}$ and $F_{3,4}$ are assigned to the split FSs at Γ and L, respectively. However, it is difficult to assign F_5 - F_8 since the sizes of the FSs at K and A are close. We derive the Fermi velocities from the FFT spectra at different temperatures in the Supplementary Information. By comparing them with those of the band dispersions recorded by ARPES, we assign $F_{5,7}$ and $F_{6,8}$ to the split FSs at K and A, respectively.

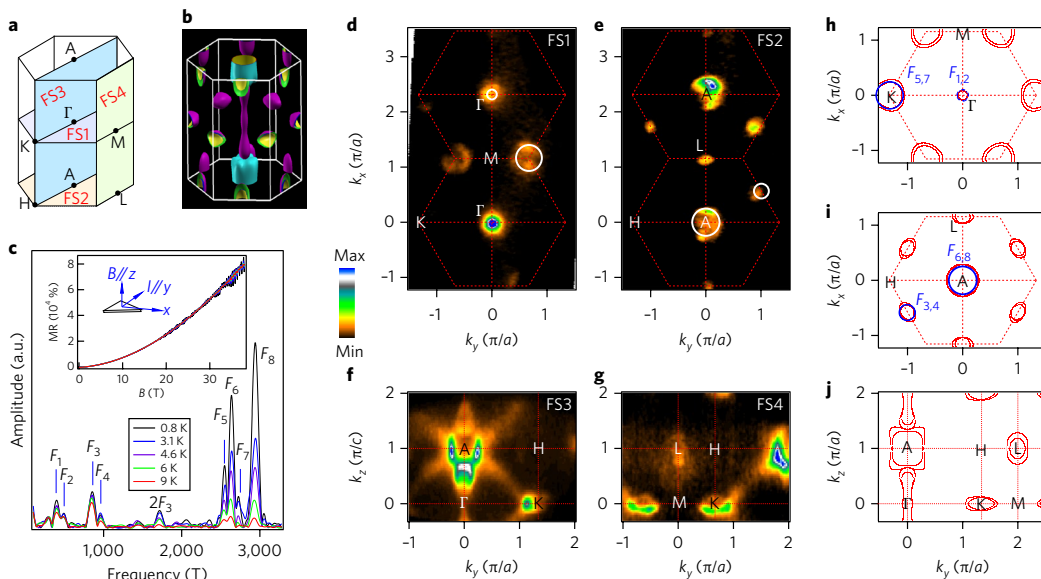


Fig. 2 | FSs in the (001) and (100) planes of WC. **a**, Bulk BZ with four planes, which indicate the locations of the measured FSs in **d–g**. **b**, Calculated 3D bulk FSs in the bulk BZ. **c**, FFT spectra computed over a field window of 21–38 T of the QO data taken at several temperatures, showing eight principal frequencies F_1 to F_8 . The inset shows magnetoresistance as a function of B at different temperatures, in which the ripples show quantum oscillations. The electric current I and B are parallel to the [010] and [001] directions, respectively. **d–g**, Photoemission intensity plots at E_F , showing FSs in the four high-symmetry planes indicated in **a**. The data in **d** and **e** were recorded on the (001) cleavage surface with $h\nu = 445$ and 536 eV, respectively. The data in **f** and **g** were recorded on the (100) cleavage surface with $h\nu = 555$ and 351 eV, respectively. All of the data in **d** to **g** were taken with linearly horizontal polarized light. **h–j**, Calculated bulk FSs in the four high-symmetry planes. The blue circles are an isotropic fitting of the cross-sectional areas corresponding to the eight frequencies F_1 – F_8 in **c**. The splitting of the FS circles is too small to be observed by eye.

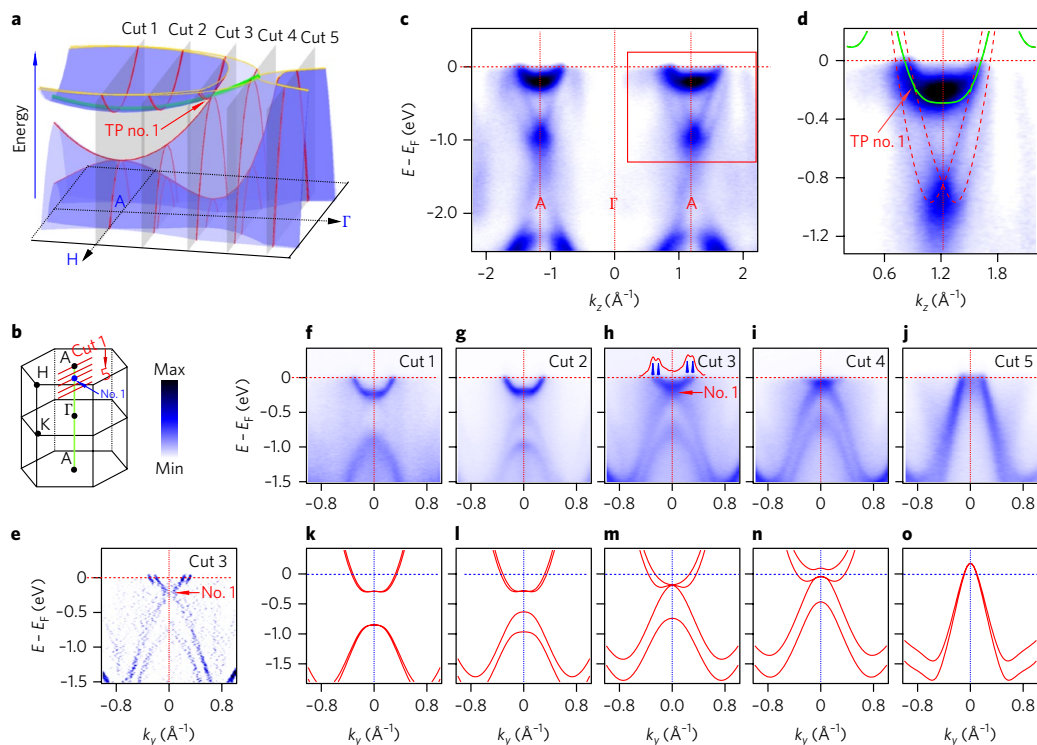


Fig. 3 | Band dispersions near TP no. 1. **a**, Schematic 3D plot of the electronic structure near TP no. 1 in the $k_x = 0$ plane. The grey planes indicate the locations of cuts 1 to 5 in **f–j**. The red and green curves represent the singly and doubly degenerate bands, respectively. The yellow curves represent the FSs. **b**, Bulk BZ with red and green lines indicating the locations of cuts 1 to 5 in **f–j** and the cut in **c**, respectively. **c**, Photoemission intensity plot of band dispersions along A– Γ –A. **d**, Zoom-in of the region in the red box in **c** with the calculated bands on top of the data. **e**, Curvature intensity plot of the data in **d**. **f–j**, Photoemission intensity plots of band dispersions along cuts 1 to 5, respectively. The red curve in **h** is the momentum distribution curve at E_F along cut 3, showing double peaks indicated by blue arrows. **k–o**, Calculated bulk bands along cuts 1 to 5, respectively. The ARPES data were recorded on the (100) cleavage surface with $h\nu = 555$ eV under linearly horizontal polarization.

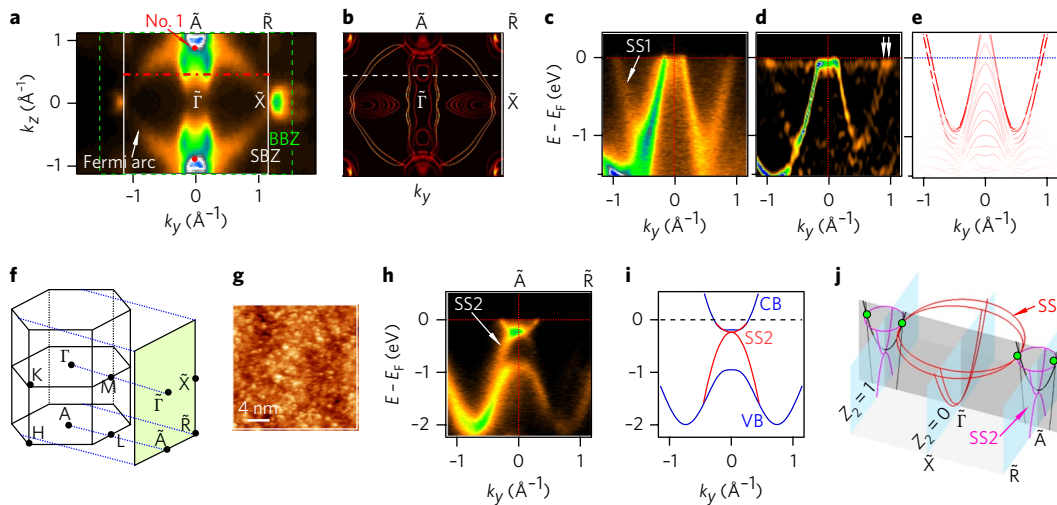


Fig. 4 | SSs on the (100) surface of WC. **a**, Photoemission intensity plot at -200 meV recorded with $h\nu=555$ eV under linearly horizontal polarization, which measures the $k_x=0$ plane of bulk BZ. The red points indicate the projection locations of TP no. 1. The white and green rectangles indicate the (100) surface BZ (SBZ) and the bulk BZ at $k_x=0$ (BBZ), respectively. **b**, Calculated SS FSs at the energy of TP no. 1 for a 15-unit-cell-thick (100) slab with the carbon-terminated layer. **c**, Photoemission intensity plot of band dispersions along the horizontal red line in **a**. **d**, Curvature intensity plot of the data in **c**, showing slight band splitting indicated by white arrows. **e**, Calculated SS bands along the horizontal white line in **b**. **f**, Bulk and (100) surface BZ with high-symmetry points. **g**, Typical STM constant-current topographic image of the in situ cleaved (100) surface under an ultrahigh vacuum (scanning parameters: $V=-1.0$ V, $I=0.4$ nA). **h**, Photoemission intensity plot recorded with $h\nu=555$ eV under right-hand circular polarization, showing band dispersions along $\tilde{\Gamma}-\tilde{R}$. **i**, Schematic band dispersions along $\tilde{\Gamma}-\tilde{R}$ showing Dirac SS bands connecting the bulk valence band (VB) and conduction band (CB). **j**, Schematic 3D plot of surface Fermi arcs connecting the surface projections of TP no. 1 (green dots) and SS bands along $\tilde{\Gamma}-\tilde{X}$ and $\tilde{A}-\tilde{R}$, which are consistent with the 2D topological properties on the $k_z=0$ and π planes.

We further investigate the FSs in the k_y-k_z planes by ARPES measurements on the (100) surface. The calculated bulk FSs in the k_y-k_z plane (Fig. 2j) are consistent with our observation in Fig. 2f,g, although the FS splitting is not resolved experimentally. In addition, we observe almost straight FS lines in Fig. 2f,g, which are absent in the calculated bulk FSs. The $h\nu$ dependence measurements (Supplementary Fig. 1) show that the extra feature has a constant momentum location, which is an indication of SSs. Its spectral intensity is strongly modulated with a periodicity in agreement with the bulk BZ. This indicates that the SSs are strongly hybridized with the bulk states. Next we demonstrate the presence of TPs in the bulk electronic structure of WC (Fig. 3) and discuss the topological properties of the SSs (Fig. 4).

The band calculations indicate that only TP no. 1 is located below E_F (Fig. 1c). A schematic three-dimensional (3D) plot of the band structure near TP no. 1 in the $k_x=0$ plane is displayed in Fig. 3a. To search for the theoretically proposed TP no. 1, we have systematically measured the band dispersions on the (100) surface. The ARPES data along $\tilde{\Gamma}-\tilde{A}$ in Fig. 3c exhibit three electron bands around A. In Fig. 3d, we overlap the calculated band structure on top of the experimental data around A. According to the Kramers theorem, the bands must be spin-degenerate at the time-reversal invariant momentum A. The calculations in Fig. 3d show that the two deep bands are degenerate at A and exhibit Rashba-like splitting on dispersing towards $\tilde{\Gamma}$, whereas the shallow band remains doubly degenerate along the $\tilde{\Gamma}-\tilde{A}$ direction, which is protected by the vertical mirror symmetry M_y . The doubly degenerate band crosses the inner singly degenerate band at ~ 200 meV below E_F , which produces TP no. 1. The calculated band structure, especially the band crossing, is fully consistent with our experimental band dispersions, confirming the presence of TP no. 1 in the electronic structure of WC.

To further characterize TP no. 1, we measured the band dispersions perpendicular to $\tilde{\Gamma}-\tilde{A}$. Figure 3f-j shows the experimental

band dispersions along five representative cuts at different k_z values, whose momentum locations are illustrated in Fig. 3a,b. We observe one electron band and one hole band along cut 1 ($k_z=\pi$) in Fig. 3f. The hole band splits into two bands when sliding the cut away from $k_z=\pi$. The upper hole band touches the electron band at ~ 200 meV below E_F along cut 3 (Fig. 3h). We further resolve double peaks from the momentum distribution curve at E_F in Fig. 3h, which is supported by the curvature intensity plot in Fig. 3e. This indicates that the electron band dispersion consists of two nearby bands. The experimental band dispersions are well reproduced by our calculations in Fig. 3m, which show that two electron bands and one hole band are touching at one point along cut 3. This consistency between experiment and calculation provides further evidence for the presence of TP no. 1.

Next, we prove the non-trivial topology of the semimetal state in WC by investigating the SSs observed on the (100) surface. As the disordered top layer does not have a well-defined band structure, the SSs that we observe should lie on the boundary of the ordered lattice, which is beneath the disordered layer.

The intensity map at 200 meV below E_F , corresponding to the energy of TP no. 1, shows that the FS lines enter into the bulk states at the projection points of TP no. 1 (Fig. 4a). A similar feature is also observed in our slab calculations (Fig. 4b), although the calculations cannot simulate the real surface covered by a disordered layer. The calculations reveal two pairs of Fermi arcs, which are the constant-energy contours of two nearly parallel SS bands, as seen in Fig. 4e. A slight splitting of the SS bands is also observed in our experimental data (Fig. 4c,d), suggesting that the observed FS lines are composed of two pairs of Fermi arcs, which are indicated as SS1 in Fig. 4j. To understand the surface Fermi arcs, we investigate the 2D topological property on the $k_z=0$ plane (see details in the Supplementary Information). This is because the Fermi arcs cross the (100) surface projection line $\tilde{\Gamma}-\tilde{X}$ of the time-reversal invariant $k_z=0$ plane, so that they are dictated by the bulk band topology on the $k_z=0$ plane^{35,36}. The

topological invariant Z_2 for the $k_z=0$ plane is found to be trivial, meaning that there are pairs of SS bands between $\tilde{\Gamma}$ and \tilde{X} , which constitute the double pairs of Fermi arcs, as illustrated in Fig. 4j.

By contrast, our calculations show that the time-reversal invariant $k_z=\pi$ plane has a non-trivial topological invariant $Z_2=1$ (Supplementary Fig. 2), and thus gapless Dirac SS bands connecting the bulk valence and conduction bands should appear along $\tilde{A}-\tilde{R}$ (refs^{35,36}). In Fig. 3f, we observe a hole band that almost touches the bulk electron band at A, but its spectral intensity recorded with linearly horizontal polarized light is very low. Using right-hand circular polarized light, the spectral intensity of the hole band is substantially enhanced, as shown in Fig. 4h. Our $h\nu$ dependence measurements indicate that the hole band is also SSs, which is strongly hybridized with the bulk states. Since no other SSs are observed along $\tilde{A}-\tilde{R}$, we attribute the hole band to the lower branch of the expected surface Dirac bands. This means that the surface Dirac node at \tilde{A} is very close to the bottom of bulk conduction bands (Fig. 4i) and therefore the upper branch is difficult to resolve. However, the non-trivial topology in the $k_z=\pi$ plane guarantees the existence of the upper branch. The constant-energy contour of the upper branch constitutes either a closed FS circle enclosing \tilde{A} or a pair of Fermi arcs connecting to the surface projections of two TP no. 1 points on both sides of the surface BZ boundary, which is indicated as SS2 in Fig. 4j.

Our results suggest that three pairs of Fermi arcs emanate from the (100) surface projection of TP no. 1 (Fig. 4j). We note that the SS1 is topologically distinct from the SS2. As the $k_z=0$ plane has a trivial topological invariant $Z_2=0$, the existence of SS1 is not guaranteed and it can be fully removed by continuous deformation^{35,36}. By contrast, the $k_z=\pi$ plane has a non-trivial topological invariant $Z_2=1$, which guarantees the existence of gapless Dirac SS bands along $\tilde{A}-\tilde{R}$ ^{35,36}. Therefore, the SS2 can be deformed into a closed FS enclosing \tilde{A} but cannot be fully removed. With the observation of topological SSs in WC, we prove the non-trivial topology of the new type of semimetal state beyond Dirac and Weyl semimetals.

Finally, we mention that the three-component fermions observed in WC are essentially distinct from the chiral fermions enforced by filling and symmetry in the non-symmorphic systems^{4,10,11,18}, in which the non-zero topological charges protect the Weyl-type Fermi arcs. In the latter case, the bulk nodes with opposite topological charges are pinned at either the centre or the corner of the bulk BZ, and thus the surface Fermi arcs connecting their projections can span over a wider segment of the surface BZ. As far as we know, all of the topological semimetals experimentally identified are driven by band inversion and the effects of SOC. The discovery of symmetry-enforced topological semimetals calls for future experimental efforts.

Methods

Methods, including statements of data availability and any associated accession codes and references, are available at <https://doi.org/10.1038/s41567-017-0021-8>.

Received: 14 June 2017; Accepted: 9 November 2017;

Published online: 08 January 2018

References

1. Wan, X., Turner, A. M., Vishwanath, A. & Savrasov, S. Y. Topological semimetal and Fermi-arc surface states in the electronic structure of pyrochlore iridates. *Phys. Rev. B* **83**, 205101 (2011).
2. Wang, Z. et al. Dirac semimetal and topological phase transitions in A_3Bi ($A=Na, K, Rb$). *Phys. Rev. B* **85**, 195320 (2012).
3. Wieder, B. J., Kim, Y., Rappe, A. M. & Kane, C. L. Double Dirac semimetals in three dimensions. *Phys. Rev. Lett.* **116**, 186402 (2016).
4. Bradlyn, B. et al. Beyond Dirac and Weyl fermions: Unconventional quasiparticles in conventional crystals. *Science* **353**, 558 (2016).
5. Heikkilä, T. T. & Volovik, G. E. Nexus and Dirac lines in topological materials. *New J. Phys.* **17**, 093019 (2015).

6. Weng, H., Fang, C., Fang, Z. & Dai, X. Topological semimetals with triply degenerate nodal points in θ -phase tantalum nitride. *Phys. Rev. B* **93**, 241202 (2016).
7. Zhu, Z., Winkler, G. W., Wu, Q., Li, J. & Soluyanov, A. A. Triple point topological metals. *Phys. Rev. X* **6**, 031003 (2016).
8. Weng, H., Fang, C., Fang, Z. & Dai, X. Coexistence of Weyl fermion and massless triply degenerate nodal points. *Phys. Rev. B* **94**, 165201 (2016).
9. Chang, G. et al. Nexus fermions in topological symmorphic crystalline metals. *Sci. Rep.* **7**, 1688 (2017).
10. Chang, G. et al. Unconventional Chiral Fermions and Large Topological Fermi Arcs in RhSi. *Phys. Rev. Lett.* **119**, 206401 (2017).
11. Tang, P., Zhou, Q. & Zhang, S. C. Multiple types of topological fermions in transition metal silicides. *Phys. Rev. Lett.* **119**, 206402 (2017).
12. Castro Neto, A. H., Guinea, F., Peres, N. M. R., Novoselov, K. S. & Geim, A. K. The electronic properties of graphene. *Rev. Mod. Phys.* **81**, 109–162 (2009).
13. Fu, L. & Kane, C. L. Superconducting proximity effect and majorana fermions at the surface of a topological insulator. *Phys. Rev. Lett.* **100**, 096407 (2008).
14. Fang, Z. et al. The anomalous Hall effect and magnetic monopoles in momentum space. *Science* **302**, 92–95 (2003).
15. Weng, H. M., Fang, C., Fang, Z., Bernevig, B. A. & Dai, X. Weyl semimetal phase in noncentrosymmetric transition-metal monophosphides. *Phys. Rev. X* **5**, 011029 (2015).
16. Huang, S.-M. et al. A Weyl fermion semimetal with surface Fermi arcs in the transition metal monophosphide TaAs class. *Nat. Commun.* **6**, 7373 (2015).
17. Soluyanov, A. A. et al. Type-II Weyl semimetals. *Nature* **527**, 495–498 (2015).
18. Chang, G. et al. Kramers–Weyl fermions. Preprint at <https://arxiv.org/abs/1611.07925> (2016).
19. Liu, Z. K. et al. Discovery of a three-dimensional topological Dirac semimetal Na_3Bi . *Science* **343**, 864–867 (2014).
20. Lv, B. Q. et al. Experimental discovery of Weyl semimetal TaAs. *Phys. Rev. X* **5**, 031013 (2015).
21. Xu, S. Y. et al. Discovery of a Weyl fermion semimetal and topological Fermi arcs. *Science* **349**, 613–617 (2016).
22. Lv, B. Q. et al. Observation of Weyl nodes in TaAs. *Nat. Phys.* **11**, 724–727 (2015).
23. Yang, L. X. et al. Weyl semimetal phase in the non-centrosymmetric compound TaAs. *Nat. Phys.* **11**, 728–732 (2015).
24. Xu, S.-Y. et al. Observation of Fermi arc surface states in a topological metal. *Science* **347**, 294–298 (2015).
25. Potter, A. C., Kimchi, I. & Vishwanath, A. Quantum oscillations from surface Fermi arcs in Weyl and Dirac semimetals. *Nat. Commun.* **5**, 5161 (2014).
26. Kargarian, M., Randeria, M. & Lu, Y.-M. Are the surface Fermi arcs in Dirac semimetals topologically protected? *Proc. Natl Acad. Sci. USA* **113**, 8648–8652 (2016).
27. Fang, C., Lu, L., Liu, J. & Fu, L. Topological semimetals with helicoid surface states. *Nat. Phys.* **12**, 936–941 (2016).
28. Lv, B. Q. et al. Observation of three-component fermions in the topological semimetal molybdenum phosphide. *Nature* **546**, 627–631 (2016).
29. Shekhar, C. et al. Extremely high conductivity observed in the unconventional triple point fermion material MoP. Preprint at <https://arxiv.org/abs/1703.03736> (2017).
30. He, J. B. et al. Magnetotransport properties of the triply degenerate node topological semimetal tungsten carbide. *Phys. Rev. B* **95**, 195165 (2017).
31. Xiong, J. et al. Evidence for the chiral anomaly in the Dirac semimetal Na_3Bi . *Science* **350**, 413–416 (2015).
32. Huang, X. et al. Observation of the chiral-anomaly-induced negative magnetoresistance in 3D Weyl semimetal TaAs. *Phys. Rev. X* **5**, 031023 (2015).
33. Strocov, V. N. et al. Three-dimensional electron realm in VSe₂ by soft X-ray photoelectron spectroscopy: origin of charge-density waves. *Phys. Rev. Lett.* **109**, 086401 (2012).
34. Shoenberg, D. *Magnetic Oscillations in Metals* (Cambridge Univ. Press, Cambridge, 1984).
35. Kane, C. L. & Mele, E. J. Z_2 topological order and the quantum spin Hall effect. *Phys. Rev. Lett.* **95**, 146802 (2005).
36. Fu, L., Kane, C. L. & Mele, E. J. Topological insulators in three dimensions. *Phys. Rev. Lett.* **98**, 106803 (2007).

Acknowledgements

We acknowledge G. Li for valuable discussion. This work was supported by the Ministry of Science and Technology of China (2016YFA0300600, 2016YFA0401000, 2016YFA0302400, 2015CB921300, 2013CB921700, 2016YFA0202301 and 2016YFA0300300), the National Natural Science Foundation of China (11622435, 11474340, 11422428, 11674369, 11234014, 11404175, 61725107 and 11674371) and the Chinese Academy of Sciences (XDB07000000 and XDB06). Y.-B.H. acknowledges funding from the CAS Pioneer

Hundred Talents Program (type C). A portion of this work performed at the National High Magnetic Field Laboratory, Tallahassee, USA, is supported by the National Science Foundation Cooperative Agreement DMR-1157490 and the State of Florida.

Author contributions

H.D. and T.Q. conceived the ARPES experiments; J.-Z.M. and T.Q. performed ARPES measurements with the assistance of B.-Q.L., L.-Y.K., X.G., L.-Y.R. and Y.-B.H.; Y.-F.X. and H.-M.W. performed ab initio calculations; J.-B.H., D.C., W.-L.Z. and G.-F.C. synthesized the single crystals; S.Z., D.C., C.-Y.X., E.S.C. and G.-F.C. performed quantum oscillation measurements; J.-Z.M., T.Q. and H.D. analysed the experimental data; J.-Z.M., Y.-F.X., T.Q. and J.-B.H. plotted the figures; X.D. discussed the experimental and calculated data; Y.S., J.-Z.M., Y.-L.W. and H.-J.G. performed STM experiments. T.Q., C.F., H.-M.W., H.D., J.-Z.M. and P.R. wrote the manuscript.

Competing interests

The authors declare no competing financial interests.

Additional information

Supplementary information is available for this paper at <https://doi.org/10.1038/s41567-017-0021-8>.

Reprints and permissions information is available at www.nature.com/reprints.

Correspondence and requests for materials should be addressed to G.-F.C., T.Q. and H.D.

Publisher's note: Springer Nature remains neutral with regard to jurisdictional claims in published maps and institutional affiliations.

Methods

Sample growth. High-quality single crystals of WC were grown by the flux method³⁰. The starting materials, W, C and Co, were mixed in the ratio of 1:1:5, and placed in a graphite crucible with a cap. The crucible was heated to 1,700°C, held for 50 h, and then cooled to 1,400°C at a rate of 1°C h⁻¹ in an argon atmosphere. The Co flux was then removed by dissolving in a warm hydrochloric acid solution. The obtained single crystals are in the form of equilateral triangles with sides of 3 mm and thickness of 0.3 mm. The crystal structure was characterized by X-ray diffraction using a PANalytical diffractometer with CuK_α radiation at room temperature. The elemental compositions were checked by Oxford X-Max energy dispersive X-ray spectroscopy analysis in a Hitachi S-4800 scanning electron microscope³⁰.

ARPES and quantum oscillation measurements. Soft x-ray ARPES measurements were performed at the 'Dreamline' beamline of the Shanghai Synchrotron Radiation Facility with a Scienta Omicron DA30L analyser. The energy and angular resolutions were set to 60–100 meV and 0.2°, respectively. The samples for ARPES measurements were cleaved in situ and measured at 30 K in a vacuum better than 5×10^{-11} torr. High-field magnetoresistance oscillation was measured on the bar specimen by a standard four-point probe technique at the Steady High Magnetic Field Facilities, High Magnetic Field Laboratory, Chinese Academy of Sciences and at the National High Magnetic Field Laboratory, Tallahassee, USA.

Calculation. WC is crystallized in a hexagonal lattice with space group $P\bar{6}m2$ (no. 187). The lattice constants $a = b = 2.918$ Å, and $c = 2.846$ Å are adopted in our calculations. The W and C atoms are located at Wyckoff positions $1d$ (1/3, 2/3, 1/2)

and $1a$ (0, 0, 0), respectively. The Vienna Ab initio Simulation Package (VASP)^{37,38} with the generalized gradient approximation–Perdew, Burke and Ernzerhof (PBE–GGA)-type exchange correlation potential is employed in our first-principles calculations³⁹. The plane-wave cutoff energy is 500 eV and the k -point sampling grid is $11 \times 11 \times 11$. The maximally localized Wannier functions for $5d$ orbitals on W and $2p$ orbitals on C have been constructed by using the Wannier90 package⁴⁰. SOC is taken into account in all of the above calculations. A slab with a thickness of 15 unit cells along the c lattice has been used in our (100) surface-state calculations. The slab is separated by a vacuum layer of 10 Å, above which the calculated electronic structures are converged, indicating that the interactions between different slabs are avoided sufficiently.

Data availability. The data that support the plots within this paper and other findings of this study are available from the corresponding author upon reasonable request.

References

37. Kresse, G. & Furthmüller, J. Efficiency of ab-initio total energy calculations for metals and semiconductors using a plane-wave basis set. *Comput. Mater. Sci.* **6**, 15–50 (1996).
38. Kresse, G. & Furthmüller, J. Efficient iterative schemes for ab initio total-energy calculations using a plane-wave basis set. *Phys. Rev. B* **54**, 11169 (1996).
39. Perdew, J. P., Burke, K. & Ernzerhof, M. Generalized gradient approximation made simple. *Phys. Rev. Lett.* **77**, 3865–3868 (1996).
40. Marzari, N. & Vanderbilt, D. Maximally localized generalized Wannier functions for composite energy bands. *Phys. Rev. B* **56**, 12847 (1997).